

Synthesis and Characterization of Mn-Doped ZnO Nanocrystals

Ranjani Viswanatha,[‡] Sameer Sapra,[‡] Subhra Sen Gupta,^{‡,†} B. Satpati,[§] P. V. Satyam,[§] B. N. Dev,[§] and D. D. Sarma^{*,‡}

Solid State and Structural Chemistry Unit, Indian Institute of Science, Bangalore-560012, India, and
Institute of Physics, Sachivalaya Marg, Bhubaneswar-751005, India

Received: January 5, 2004; In Final Form: February 28, 2004

We report the synthesis and characterization of several sizes of Mn-doped ZnO nanocrystals, both in the free-standing and the capped particle forms. The sizes of these nanocrystals could be controlled by capping them with polyvinylpyrrolidone under different synthesis conditions and were estimated by X-ray diffraction and transmission electron microscopy. The absorption properties of PVP-capped Mn-doped ZnO exhibit an interesting variation of the band gap with the concentration of Mn. Fluorescence emission, electron paramagnetic resonance, and X-ray absorption spectroscopy provide evidence for the presence of Mn in the interior as well as on the surface of the nanocrystals.

I. Introduction

Dilute magnetic semiconductors (DMSs) have attracted a great deal of attention in the past few years as enabling materials in the emerging field of “spintronics”.¹ DMSs are semiconductor solid solutions, where a small percentage of cations are replaced by magnetic impurities such as Mn. Due to the host sp–Mn d interactions in these DMSs, unusual magnetotransport and magneto-optical phenomena like large Faraday rotations, giant negative magnetoresistances, and magnetic field induced metal–insulator transitions have been observed.² Among the DMSs, Mn-doped II–VI compounds have been extensively studied.³ However, most of the II–VI compounds studied are chalcogenides; the corresponding oxides are comparatively less investigated.

Bulk ZnO is a well-known wide band gap (3.3 eV) semiconducting material. In recent times, bulk ZnO has attracted increasing attention as it is a potentially useful material for a wide range of applications, such as solar cells, luminescent devices, and chemical sensors.⁴ Studies have been carried out to fine-tune the properties of ZnO to adopt it for different applications; for example, the band gap of ZnO is modified to use as UV detectors and emitters.⁵ Doping Mn into the bulk ZnO matrix offers an interesting way to alter various properties,^{6,7} for example, the band gap of the host material can be tuned from 3.3 eV to 3.7 eV. Additionally, it also alters the emission properties by providing an efficient channel for the recombination of the electron and the hole via the dopant Mn d levels. The optical and electronic properties of semiconductors can be further tuned by varying the size of the particles in the range below 10 nm. Additionally, it is recently reported⁸ that Mn-doped ZnO thin films as well as in bulk exhibit ferromagnetism at room temperature. Studies on various Mn-doped semiconductor nanocrystals⁹ have revealed that the properties

of these samples, like the band gap, are influenced by the quantum confinement of electronic states; accordingly, these properties of the doped nanocrystals are considerably different compared to those of the doped bulk system.¹⁰ These interesting changes in confined DMSs have enlarged the scope of research activity in this field, prompting us to study the confinement effects in Mn-doped ZnO nanocrystals.

While it has been known¹¹ for a while that it is possible to produce free-standing ZnO nanocrystals, synthesizing such free-standing ZnO nanocrystals doped with a transition metal ion has been realized only recently by doping with Co.¹² We have been pursuing the synthesis of good quality free-standing ZnO nanocrystals doped with other transition metal ions by exploring various synthetic routes. Here we report for the first time the synthesis and characterization of Mn-doped free-standing ZnO nanocrystals with a particle size of a few nanometers. While the diameter of these free-standing particles varied from ~5 nm to ~10.5 nm, to obtain smaller particles and a good control over the size, we have capped Mn-doped ZnO nanocrystals with polyvinylpyrrolidone (PVP). These nanocrystals are characterized using energy dispersive analysis of X-rays (EDAX), inductively coupled plasma atomic emission spectrometry (ICP-AES), X-ray diffraction (XRD), transmission electron microscopy (TEM), and ultraviolet–visible (UV–vis) absorption spectroscopy. Fluorescence spectroscopy (PL), electron paramagnetic resonance (EPR), and X-ray absorption spectroscopy (XAS) have been used to probe the nature of doped Mn ions in the ZnO nanocrystal matrix.

II. Experimental Section

Materials. Zinc acetate dihydrate ($\text{Zn}(\text{OAc})_2 \cdot 2\text{H}_2\text{O}$) (Ranbaxy), manganese acetate tetrahydrate ($\text{Mn}(\text{OAc})_2 \cdot 4\text{H}_2\text{O}$) (Ranbaxy), PVP (Aldrich, MW 10 000), sodium hydroxide (NaOH) (Ranbaxy), and isopropyl alcohol (*i*-PrOH) (Merck) were used as received. Double-distilled water was employed for all experiments.

Synthesis. In a typical synthesis of the Mn-doped ZnO nanocrystals, the required amount of $\text{Mn}(\text{OAc})_2 \cdot 4\text{H}_2\text{O}$ was dissolved in 1 mL of water. This solution was added to 100 mL of the solvent, *i*-PrOH, under vigorous stirring. After

* Corresponding author. E-mail: sarma@sscu.iisc.ernet.in. Also at the Jawaharlal Nehru Centre for Advanced Scientific Research, Jakkur, Bangalore-560064, India.

[‡] Indian Institute of Science.

[§] Institute of Physics.

[†] Also at the Department of Physics, Indian Institute of Science, Bangalore-560012, India.

TABLE 1: Amounts of Reactants Required to Prepare Nanocrystals with Different Manganese Concentrations

chemicals	amounts added in mmol for			
	0% Mn	2% Mn	5% Mn	10% Mn
Zn(OAc) ₂ ·2H ₂ O	0.50	0.49	0.475	0.45
Mn(OAc) ₂ ·4H ₂ O	0.0	0.01	0.025	0.05
NaOH	1.25	1.25	1.25	1.25
PVP	0.30	0.30	0.30	0.30

maintaining the reaction mixture for a couple of hours at room temperature, Zn(OAc)₂·2H₂O was added, and the mixture was heated to 50 °C. It was then quenched in ice, and PVP was added. The reaction mixture was stirred for a few hours and then hydrolyzed by the dropwise addition of NaOH solution in *i*-PrOH (125 mM) under ultrasonic agitation for about 2 h. The solvents were then removed by rotavaporization. The resulting mixture was washed with water leading to the precipitation of Zn_{1-x}Mn_xO nanocrystals. The precipitate was centrifuged and dried in a vacuum for 10 h. The amounts of the chemicals used to synthesize these nanocrystals doped with different concentrations of Mn are given in Table 1. A similar method of preparation, without the addition of PVP, was used to synthesize free-standing uncapped ZnO and Mn-doped ZnO nanocrystals.

Structural Characterization. The percentages of Mn present in the final samples were estimated by EDAX analysis with a JEOL JSM-840A model, after coating the samples with gold, to avoid charging and melting of the PVP layers. The percentages of Mn were determined more precisely using ICP-AES with a Jobin Yvon-24 model. The average particle size and crystal structure identification of the particles were determined from X-ray diffraction patterns that were recorded on a Siemens D5005 diffractometer using Cu K α radiation. Since the diffracted intensities from these nanocrystals are generally weak, all patterns were recorded at a slow scan rate (0.75° per min) in order to get a high signal-to-noise ratio. The size distribution of the nanocrystals in these samples was determined from TEM images obtained using a JEOL 2010F UHR version electron microscope at an accelerating voltage of 200 kV. Samples for TEM were prepared by making a clear dispersion of the nanocrystals in methanol and putting a drop of the solution on a carbon-coated copper grid. The solution was allowed to evaporate leaving behind the nanocrystals on the carbon grid. The powder samples of Mn-doped ZnO nanocrystals were dissolved in *i*-PrOH, and the band gaps were determined from the optical absorption spectra obtained using a Perkin-Elmer double-beam Lambda-35 spectrophotometer. Pure *i*-PrOH was used as the reference blank solution for the samples. Fluorescence spectra were obtained using a Perkin-Elmer LS-55 spectrofluorophotometer after dissolving the powders in *i*-PrOH. EPR spectra of the powder samples of Mn-doped ZnO were recorded on an ER 200D X-band Bruker instrument. X-ray absorption spectra at the Mn L_{2,3} edge were measured at the BEAR beamline using the synchrotron radiation source, Elettra, Trieste operated at an energy of 2.0 GeV with a resolution of 0.5 eV by measuring the drain current.

Theoretical Calculations. The theoretical 2p \rightarrow 3d XAS of Mn in Mn-doped ZnO was calculated using the Lanczos iterative algorithm of a many body Hamiltonian, based on a fully coherent spectral function for the (MnO₄)⁶⁻ tetrahedral cluster corresponding to the wurtzite structure. The details of the theoretical approach can be found elsewhere.¹³ The calculations were performed with complete Mn 3d–3d and 2p–3d multiplet interactions, corresponding to average values (U_{dd} and U_{pd}) of 7.0 eV and 8.4 eV, respectively. The charge transfer energy (Δ) was taken to be 6.5 eV in accordance with the published

TABLE 2: Nominal Mn Concentration in the Reaction Mixture and the Concentration as Determined by EDAX/ICP-AES Analysis

Mn % nominal	2	5	10
Mn % EDAX	0.9	2.3	5
Mn % ICP-AES	0.4	1.8	4

data.¹⁴ The scaled hopping parameters used for MnO were¹⁵ $pp\sigma = 0.239$ eV, $pp\pi = -0.098$ eV, $pd\sigma = -1.329$ eV, and $pd\pi = 1.024$ eV. We also include a crystal field effect, where the strength was adjusted to obtain the best description of the experimental data. The spectrum thus obtained was broadened by a Gaussian function of width 0.5 eV to simulate instrumental broadening and a Lorentzian function of width 0.55 eV (for the L₃ region) and 0.60 eV (for the L₂ region) to account for the finite lifetime of the core hole.

III. Results and Discussion

Table 2 gives a comparison of the nominal percentage of Mn added, the percentage of Mn as determined by EDAX analysis, and the percentage of Mn as determined by ICP-AES for PVP-capped Zn_{1-x}Mn_xO nanocrystals. It was found that the error bar associated with the EDAX measurements was about $\pm 2\%$. Hence, the ICP-AES analysis was carried out, and the results were found to match quite well with the EDAX analysis. It is seen that the amount of Mn incorporated into the ZnO matrix is a little less than half the actual amount of Mn added during the synthesis; this may be due to the low solubility of Mn(OAc)₂·4H₂O in *i*-PrOH (sparingly soluble in comparison to 2 g/100 cm³ of the corresponding Zn salt), which is used as a solvent in the synthesis procedure.

Structure and Size. X-ray Diffraction. The XRD pattern obtained for the free-standing ZnO nanocrystals is shown with open circles in plot i of Figure 1. Comparing the result with the XRD pattern of bulk ZnO crystallizing in the wurtzite phase (plot vi in the figure), we observe that the positions and intensities of the diffraction peaks for the nanocrystal samples are in agreement with those of bulk ZnO, demonstrating the formation of wurtzite nanocrystals with similar lattice parameters as in the bulk. The comparison of plot i with plot vi in Figure 1 makes obvious the difference in the widths of the diffraction peaks arising from the nanocrystals and those from the bulk ZnO. The broad peaks observed in the XRD pattern of the nanocrystals arise from the finite number of diffracting planes within the finite size of the particle; the broadening in these cases is given by the Scherrer formula.¹⁶ In order to obtain more quantitative information on the size of the nanocrystals, the XRD pattern of the bulk ZnO was convoluted with a Gaussian function, whose full width at half-maximum (fwhm) was determined by the Scherrer formula, $B = 0.9\lambda/L \cos \theta$ where B , the fwhm of the diffracted peak at θ , recorded using X-rays with the wavelength λ , is related to the coherence length L . Assuming that the particles are spherical in shape, the diameter D is related to L as $D = 4L/3$. We carried out a least-squared-error approach to describe the experimental XRD patterns of the nanocrystals, in terms of the convolution of the bulk XRD pattern with the aforementioned Gaussian, using L as the fitting parameter. We found that $D = 5.3$ nm for ZnO nanocrystals provides the best description; the corresponding simulated XRD pattern is shown as a solid line in plot ii of Figure 1. On addition of 0.5 mL of water during the synthesis, we obtain bigger ZnO nanocrystals as observed by the XRD pattern (plot iii in Figure 1) compared to the XRD pattern obtained from 5.3 nm nanocrystals (plot i in Figure 1). This observation is consistent with the observation of Meulenkamp¹¹ on the role of water in

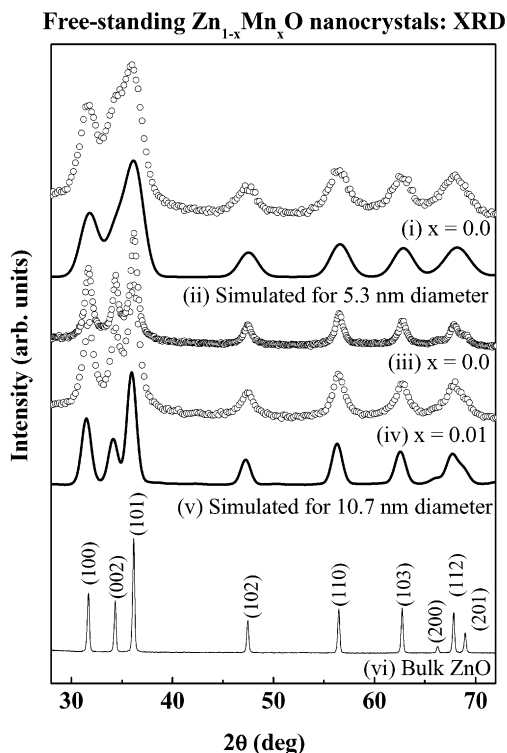


Figure 1. XRD patterns of free-standing ZnO (plots i and iii) and Mn-doped ZnO (plot iv) nanocrystals, along with the simulated XRD pattern obtained for 5.3 nm (plot ii) and 10.7 nm (plot v) particles. The XRD pattern of bulk ZnO (plot vi) is also shown for comparison.

determining the size of ZnO nanocrystals. By carrying out a similar least-squared-error fitting approach, we calculate the size of the ZnO nanocrystals obtained by the addition of water as 10.7 nm. The XRD pattern of free-standing $\text{Zn}_{0.99}\text{Mn}_{0.01}\text{O}$ (plot iv) also shows peaks corresponding to the wurtzite structure of ZnO and broadening identical to the ZnO nanocrystals (plot iii). Hence, the size of Mn-doped ZnO free-standing nanocrystals is identical to that of the ZnO free-standing nanocrystals synthesized with the same water content.

These results establish the feasibility of synthesizing free-standing pure and Mn-doped ZnO nanocrystals by this method. Though the size of the nanocrystal can be controlled by varying the water content as shown above, this method, however, restricts the minimum size of the nanocrystal that can be isolated for further investigations. Since the regime of primary interest in these nanocrystals is below the excitonic diameter (~ 5.6 nm), we have synthesized surface-modified ZnO nanocrystals in order to stabilize the lower sizes by using PVP as the capping agent. A typical XRD pattern obtained from PVP-capped, undoped ZnO nanocrystals is shown in the inset of Figure 2; we also show the XRD from PVP alone which is responsible for the changing background in the low-angle regime. In order to facilitate comparison with the bulk ZnO and subsequent analysis, we have subtracted the PVP contribution from the XRD patterns of capped nanocrystals.

Undoped ZnO nanocrystals synthesized in the absence of water with the Zn to PVP ratio of 5:3 have been reported¹⁷ with an average size of 3.5 nm. However, in order to be consistent with the synthesis of Mn-doped ZnO that requires the presence of water, we have synthesized undoped and 0.4%, 1.8%, and 4% Mn-doped ZnO nanocrystals with the same amount of water and a Zn to PVP ratio of 5:3. The resulting XRD patterns from the undoped (plot i) and a typical doped sample (plot ii) are shown in Figure 2. The extent of broadening observed for the

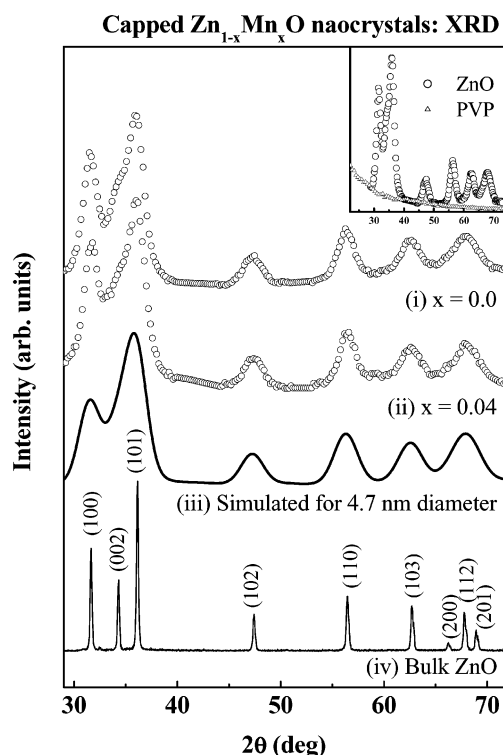


Figure 2. XRD patterns of passivated ZnO (plot i) and Mn-doped ZnO (plot ii) nanocrystals after subtraction of the PVP contribution, along with the simulated XRD pattern obtained for 4.7 nm particles (plot iii). The inset shows the raw data obtained for ZnO nanocrystals and pure PVP.

undoped system is identical to that for the doped system even in the PVP-capped systems. By means of a least-squared-error approach as described earlier, we found that $D = 4.7$ nm provides the best description for the XRD patterns of both ZnO and $\text{Zn}_{0.96}\text{Mn}_{0.04}\text{O}$ nanocrystals. We illustrate this in Figure 2 by the simulated XRD pattern (plot iii) obtained by broadening of the XRD pattern of the bulk ZnO (plot iv) according to the Scherrer formula, corresponding to spherical particles of 4.7 nm diameter. Almost identical results were obtained for all the samples with differing Mn concentrations (0.5–4%). These results show that capped ZnO nanocrystals as well as Mn-doped ZnO nanocrystals with different Mn concentrations are of identical size at least for the low Mn concentrations that we have synthesized. Mn doping is known to influence the lattice parameters of bulk ZnO arising from the differences in the ionic sizes ($\text{Mn}^{2+} - 0.80$ Å and $\text{Zn}^{2+} - 0.74$ Å in a tetrahedral symmetry). However, due to the broadening observed in the XRD patterns of these nanocrystals, it becomes impossible to estimate any such small changes in the doped ZnO lattice.

Transmission Electron Microscopy. Parts a and b of Figure 3 show bright field images of a collection of ZnO and Mn-doped ZnO nanocrystals, respectively. The images show an abundance of nearly spherical particles whose size distribution of the ZnO nanocrystals is given by the histogram shown in Figure 3c, the histogram being obtained by analyzing several frames of similar bright field images. We find that the particles have an average size of 4.5 nm in agreement with the results obtained from X-ray diffraction studies. The size distribution shown by the histogram can be represented by a Gaussian profile with a fwhm of 1.6 nm. The high-resolution image of a single particle is shown in the inset of Figure 3a. This lattice-resolved image exhibits a typical lattice spacing of about 2.69 Å corresponding to the (101) plane of the crystal. The correspond-

Transmission electron micrograph

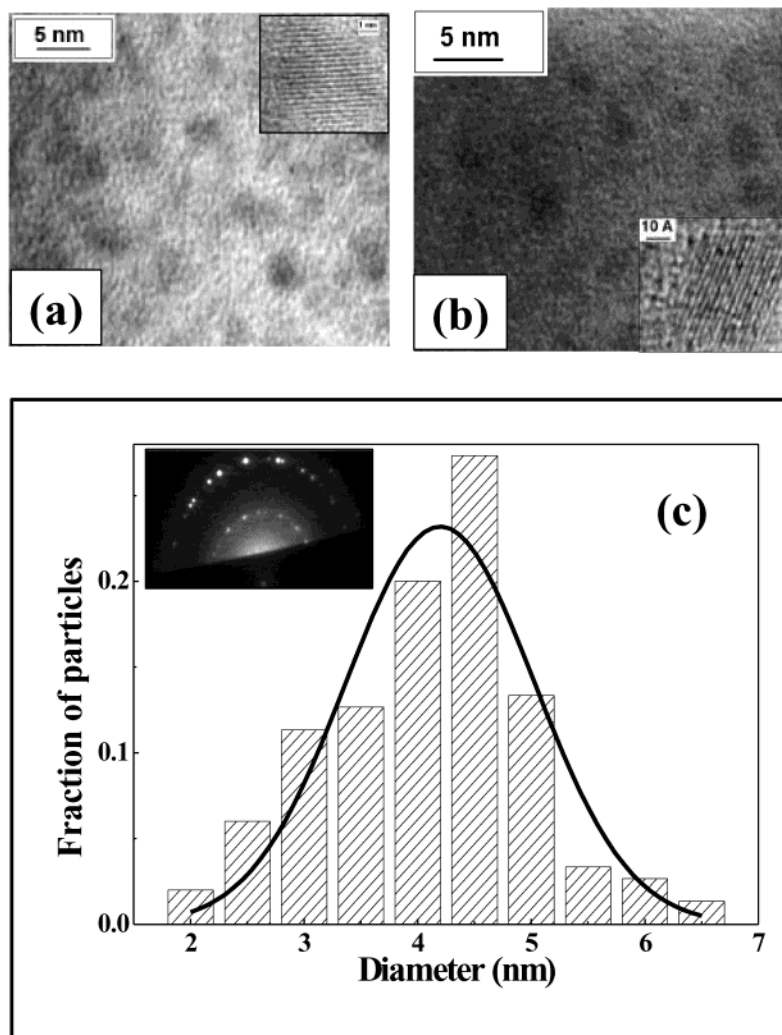


Figure 3. Bright field TEM image obtained from PVP-capped (a) ZnO nanocrystals and (b) Mn-doped ZnO nanocrystals. The insets show the corresponding high-resolution image of a single particle showing the lattice-resolved planes. (c) Histogram showing the size distribution of the ZnO nanocrystals. The inset shows the selected area electron diffraction pattern.

ing selected area electron diffraction (SAED) is shown in the inset of Figure 3c. From the SAED pattern, the nanocrystals are found to have preferential instead of random orientations.

Optical Properties. *UV–Vis Absorption Spectroscopy.* Figure 4 shows the UV-absorption spectra of free-standing ZnO and Mn-doped ZnO nanocrystals, both with an average diameter of 10.7 nm. In order to obtain a precise and quantifiable measure of the shifts in the band gaps from these absorption edges, we use the point of inflection, obtained from the minimum in the first derivative curve of the absorption spectrum. The band gap thus obtained for the ZnO nanocrystals corresponds to 3.38 eV (367 nm), indicating a blue shift of about 0.1 eV compared to the bulk band gap of 3.3 eV (373 nm), marked in the figure with an arrow, due to the quantum confinement effect. The band gap of 1% Mn-doped free-standing ZnO nanocrystals, marked by another arrow, is found to be 3.42 eV (362 nm), indicating a possible influence of Mn doping on the band gap. In order to investigate this possibility in greater detail in smaller nanocrystals, we investigated PVP-passivated samples with a fixed size (4.7 nm) of the nanocrystals as a function of the Mn content.

The inset in the Figure 5 shows the room temperature optical absorption spectra of undoped ZnO and several Mn-doped ZnO

nanocrystals. The absorption spectra from these nanocrystal samples show an increase in the band gap compared to the bulk band gap of 3.3 eV (373 nm), indicated by the pronounced blue shifts in the absorption edges of these samples. The absorption edge of the undoped sample is at 3.45 eV (360 nm); the 0.15 eV blue shift in the absorption edge compared to bulk is attributed to the quantum confinement effect. To explain this blue shift and to correlate the absorption edge with the size of the nanocrystal, we have developed a realistic and accurate tight binding (TB) scheme.^{17,18} According to these calculations, we obtain a size of 4.66 nm for the nanocrystals corresponding to the observed 0.15 eV blue shift in the absorption threshold; this is in good agreement with the size obtained from X-ray diffraction (4.7 nm) and TEM measurements (4.5 nm).

The band gap of Mn-doped ZnO nanocrystals, obtained from the inflection points of the absorption edges given in the inset of Figure 5, shows nonmonotonic dependence on the Mn concentration, as illustrated in the main frame of Figure 5. The band gap initially decreases, passes through a minimum at ~2% of Mn, and then increases with increasing Mn concentration in the nanocrystals, even though the size of the nanocrystals remains unaltered with changing Mn concentration. We have

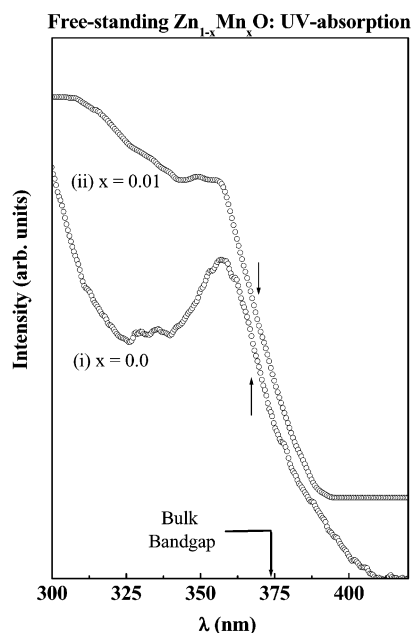


Figure 4. UV absorption curves of free-standing ZnO and $\text{Zn}_{0.99}\text{Mn}_{0.01}\text{O}$. The bulk band gap of ZnO (373 nm) and the band gap of the nanocrystals are shown by arrows.

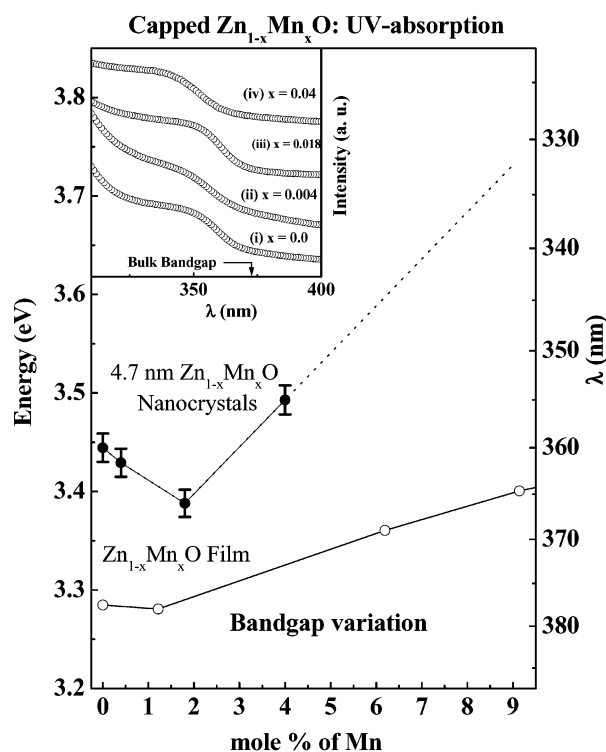


Figure 5. Variation of band gap with the percentage of Mn doping in nanocrystals (closed circles) and films (open circles) (ref 6). The inset shows the UV absorption curves of PVP-capped ZnO, $\text{Zn}_{0.996}\text{Mn}_{0.004}\text{O}$, $\text{Zn}_{0.982}\text{Mn}_{0.018}\text{O}$, and $\text{Zn}_{0.96}\text{Mn}_{0.04}\text{O}$. The bulk band gap of ZnO (373 nm) is shown by the arrow.

verified this unusual change in the band gap of fixed size ZnO nanocrystal (4.7 nm) as a function of Mn dopant concentration by reproducing the results on several independent experiments performed with different batches of samples. The error bars indicated on the data points in Figure 5 represent the variations in the results between different sets of experiments, establishing the variation in the band gap with Mn concentration to be beyond the experimental uncertainties. A similar change in the

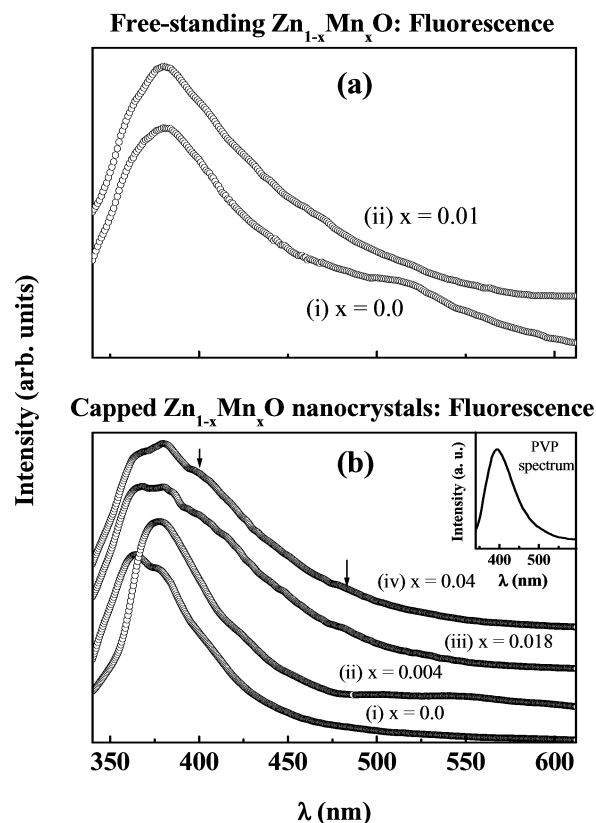


Figure 6. (a) Fluorescence spectra (obtained with $\lambda_{\text{ex}} = 325$ nm) of free-standing ZnO and Mn-doped ZnO. (b) Fluorescence spectra (obtained with $\lambda_{\text{ex}} = 325$ nm and normalized) of capped ZnO $\text{Zn}_{0.996}\text{Mn}_{0.004}\text{O}$, $\text{Zn}_{0.982}\text{Mn}_{0.018}\text{O}$, and $\text{Zn}_{0.96}\text{Mn}_{0.04}\text{O}$; the inset shows the spectrum of PVP when excited at 325 nm

band gap has also been observed in Mn-doped ZnO films,⁶ also shown in Figure 5. Interestingly, the variation of the band gap is more pronounced in the case of nanocrystals compared to the bulk system. We note that the band gap variation with the Mn concentration in doped ZnO nanocrystals is similar to that observed in Mn-doped CdS⁹ with an initial decrease of the band gap, followed by an increase; in contrast, an opposite trend of an initial increase followed by a decrease in the band gap was obtained in Mn-doped ZnS.¹⁹ It is reasonable to expect the band gap, E_g , to increase with increasing concentration of Mn, since the band gap of MnO (bulk band gap = 4.2 eV) is greater than that of ZnO (bulk band gap = 3.3 eV). However, this argument does not explain the small decrease of E_g at lower concentrations of Mn. For a short-ranged, disordered spin system (i.e., the paramagnetic phase), such a behavior, termed as band gap “bowing” has been theoretically explained using second-order perturbation theory²⁰ in the context of Mn-doped bulk ZnSe and has been attributed to strong exchange interactions present between the d electrons of Mn and the s and p electrons of the host bands. It is seen that the exchange constant involving the s-like states reduces the energy of the bottom of the conduction band ($k = 0$), and the exchange factor involving the p-like states increases the energy of the top of the valence band by a constant factor independent of temperature. These short-ranged interactions account for the anomalous decrease in the band gap for a low concentration of Mn in the system. In the spatially confined regime of the nanocrystals, these interactions are expected to be stronger, leading to more pronounced effects.

Fluorescence Spectroscopy. Figure 6a shows the fluorescence emission of free-standing ZnO and Mn-doped ZnO nanocrystals upon excitation with 325 nm photons. Undoped ZnO nanoc-

crystals exhibit two spectral features at ~ 380 nm and ~ 520 nm. The feature at ~ 380 nm corresponds to the near-band-gap emission, and the broad feature at ~ 520 nm has been attributed to surface traps.^{21–25} From the figure, it can be observed that the surface states are not very intense and the near-band-gap emission is observed even in these uncapped nanocrystals. On doping with Mn, we observe that the surface traps are significantly quenched, as indicated by a marked reduction of the emission feature at ~ 520 nm. The reduction in the surface traps results from quenching of the surface traps by the doped Mn ions. Comparison of the fluorescence spectra of the doped and the undoped samples shows there is a small increase in the spectral intensity at 420 nm and 470 nm for the doped sample. This is possibly due to the emission from the Mn ions; this interpretation is further supported by the Mn-doped ZnO nanocrystals passivated with PVP, discussed below.

Figure 6b shows the emission spectra from 4.7 nm ZnO as well as Mn-doped ZnO nanocrystals capped with PVP. The fluorescence emission spectrum from undoped ZnO nanocrystals exhibits two spectral features appearing at about 360 and 390 nm. When these are compared with the position of the absorption edge of the undoped sample (inset in Figure 5), it is evident that the 360 nm spectral feature corresponds to the band gap emission of ZnO nanocrystals. It is observed that PVP fluoresces strongly at 390 nm when excited at 325 nm, as shown in the inset of Figure 6b. Hence, the peak at 390 nm can be assigned to the presence of PVP. In this sample, the absence of the broad fluorescence band seen for free-standing ZnO nanocrystals centered at ~ 520 nm (see Figure 6a) arising from the surface trap states and observed previously even in the capped nanocrystals^{21–24} suggests that the present nanocrystal samples are well passivated.

Figure 6b also shows the effect of Mn doping on the emission properties of ZnO nanocrystals. In addition to the two peaks at about 360 nm and 390 nm, arising from the band gap and PVP emissions, respectively, one can also observe the emergence of two weak intensity, new features at about 420 nm and 480 nm marked by arrows in the figure. These transitions can be attributed to the ${}^4E \rightarrow {}^6A_1$ and ${}^4T_2 \rightarrow {}^6A_1$ transitions of Mn^{2+} ions in analogy to the case²⁶ of MnO.

Magnetic Properties. Electron Paramagnetic Resonance. Figure 7 shows EPR spectra of the doped nanocrystal samples with different Mn concentrations. The EPR spectrum from the uncapped, free-standing Mn-doped sample, shown as an inset in Figure 7, is similar to the results obtained from the samples capped with PVP, shown in the main frame of Figure 7. We note that the samples without Mn doping did not show any EPR signal, indicating the absence of any significant extent of oxygen vacancies in these samples. The spectra from the doped samples, similar to the bulk Mn-doped ZnO,²⁷ exhibit well-resolved hyperfine splitting, characteristic of isolated Mn^{2+} ions. This suggests that the Mn–Mn interactions are rather weak establishing that the Mn^{2+} ions are randomly distributed in the ZnO matrix without any significant clustering. From these spectra, we obtain the coupling constant (A) of 76 G in all cases; this value agrees well with the reported single-crystal data²⁸ obtained at 77 K. The value of the coupling constant suggests that Mn^{2+} is in a tetrahedral environment, rather than in the usually preferred octahedral environment of Mn^{2+} ions.

Each EPR spectrum in Figure 7 exhibits two sets of sextets (marked I and II in the figure), with one set shifted from the other by 39 G. From these spectra, we obtain the g -values in the Zeeman interaction term to be 2.002 (g_1) and 1.978 (g_2) corresponding to signals I and II, respectively. The value of g_1

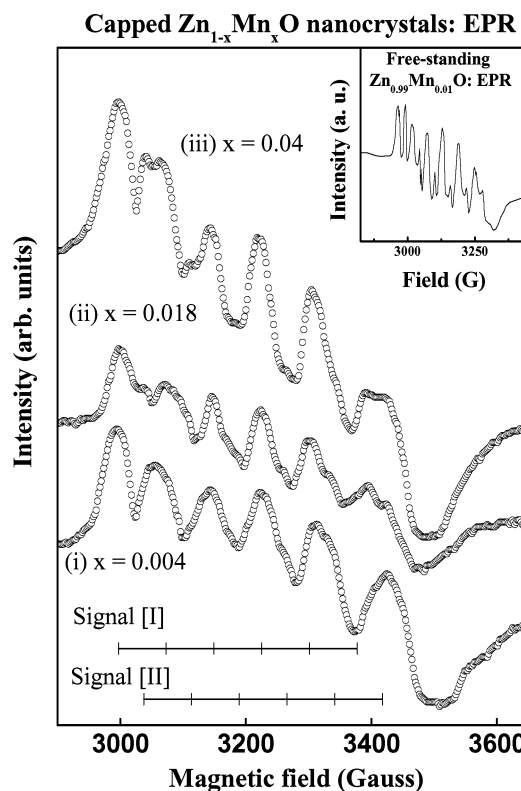


Figure 7. EPR spectra of capped $Zn_{0.996}Mn_{0.004}O$, $Zn_{0.982}Mn_{0.018}O$, and $Zn_{0.96}Mn_{0.04}O$. The inset shows the EPR spectrum of free-standing Mn-doped ZnO.

is consistent with that reported for single crystals of Mn-doped bulk ZnO.²⁸ This suggests that the chemical environment around the Mn^{2+} ion corresponding to signal I is similar to that of the single crystal, indicating the incorporation of Mn^{2+} ions at the Zn sites in the interior of the nanocrystal. Mn^{2+} ions giving rise to signal II also reside in a tetrahedral environment but with a different g -value. This suggests that the second type of Mn^{2+} ion has a somewhat different chemical environment compared to the Mn^{2+} species giving rise to signal I. It is possible that the Mn^{2+} ions giving rise to the signal II correspond to the Mn^{2+} ions on the surface of the nanocrystal. The free-standing sample (inset in Figure 7) exhibits a larger relative intensity of signal II compared to signal I. This suggests that a larger concentration of Mn resides at the surface when the surface is not passivated.

X-ray Absorption Spectroscopy. The XAS spectrum of 1.8% Mn and 4% Mn were recorded at the Mn $L_{2,3}$ edge, corresponding to the Mn $2p \rightarrow 3d$ excitations; the spectra are shown in parts a and b of Figure 8, respectively. Both the signals show the L_3 and L_2 edges of Mn centered at around 643 eV and 655 eV, respectively, confirming the presence of Mn in the samples. The $L_{2,3}$ edge of transition metal ions dominated by the local electronic structure can provide important information about its oxidation state and the point-group symmetry.²⁹ The spectrum for the 1.8% Mn-doped sample exhibits a prominent shoulder at 643 eV photon energy, besides the broad main peak at 645 eV in the L_3 region. However, the spectrum for the 4% doped sample suggests a strong reduction in the intensity of the feature at 643 eV appearing as a shoulder in the spectrum of the 1.8% sample. This indicates that the spectra in both cases are contributed to by at least two components, responsible for the two features at 643 eV and 645 eV separately; evidently the contribution with the 643 eV feature is less abundant in the 4% Mn-doped sample relative to the contribution with the 645 eV feature. These results are consistent with EPR measurements

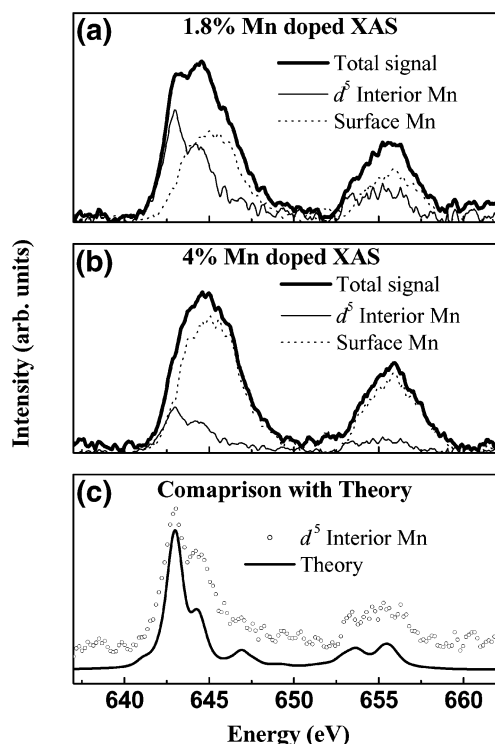


Figure 8. (a, b) XAS of 1.8% Mn and 4% Mn-doped ZnO nanocrystal, respectively, shown as thick solid lines. The decomposed spectra are shown as thin solid lines (interior Mn) and dotted lines (surface Mn). (c) Comparison of d^5 interior Mn with the theoretically calculated spectrum for a tetrahedral crystal field of 0.75 eV.

shown in Figure 7 that suggest the existence of two kinds of Mn in the system corresponding to those at the bulk (interior) and at the surface. We follow an iterative approach till self-consistency to separate the two contributions to the observed overall spectrum for both the samples; these component spectra are shown in parts a and b of Figure 8 with a thin solid line and a dashed line, respectively. Self-consistency ensures that the corresponding components are identical in both the panels, differing only in their relative weights. Noting that the component with its peak at 645 eV preferentially increases in intensity on increasing the Mn concentration, we believe that this component (dashed line in parts a and b of Figure 8) arises from Mn at or near the surface while the other component (thin solid line) is due to Mn substitutionally incorporated into the bulk of the ZnO nanocrystal. The intensity ratio of the two components suggests that only about 1% of Mn is doped into the interior of the nanocrystals for both the 1.8% and 4% Mn-doped samples with the remaining amount residing on the surface region. This is in agreement with the PL results where there is hardly any increase of the Mn related intensities between samples with 1.8% and 4% Mn-doped ZnO nanocrystals. Surprisingly, while it is possible to dope Mn in ZnO up to 33% in thin films⁶ without any phase separation, the solubility limit seems to be drastically reduced to $\sim 1\%$ in the nanocrystals.

It is to be noted that the spectral features corresponding to Mn at and near the surface region are broad, while the spectrum from Mn inside the sample exhibits sharp and distinguishable features. While Mn can be incorporated in the bulk of the nanocrystal substitutionally, thereby defining a unique site for such doped Mn ions, there are a large number of possibilities to accommodate Mn at or near the surface. Thus, the broad spectral feature of the near-surface Mn species (dashed line in Figure 8) is most likely due to a superposition of several slightly different or shifted spectral features corresponding to different

Mn sites at the surface. Thus, it becomes difficult to analyze the spectrum of the surface Mn species quantitatively. However, the characteristic features from the bulk Mn species are amenable to further analysis. In order to determine the valency, symmetry, and the crystal field strength of the Mn ions in the interior of the nanocrystals, we carried out theoretical calculations for various crystal field strengths. The spectrum that gave the best description of the experimental spectrum corresponds to a 10Dq of 0.75 eV and is shown in Figure 8c in comparison with the spectral component assigned to the Mn in the interior of the nanocrystals. The good agreement between the experimental spectrum and calculated result suggests that the doped Mn goes into the lattice with a tetrahedral MnO_4 geometry as a divalent species with a crystal field strength of about 0.75 eV.

IV. Conclusions

We have synthesized Mn-doped ZnO nanocrystals for the first time using a colloidal method with varying manganese compositions (0–4%). Free-standing, undoped ZnO nanocrystals were obtained with approximately 5.3 nm diameter in the absence of water during the synthesis, whereas the size of the nanocrystals was found to significantly increase to 10.7 nm on adding 1 mL of water during the synthesis. We have established the feasibility of doping Mn into such free-standing samples without changing the size of the nanocrystal. The size of samples prepared with the capping agent, PVP, could be controlled down to much smaller sizes and was found to be independent of the Mn concentration. The XRD patterns suggest the formation of wurtzite nanocrystals with a size of 4.7 nm in such cases. UV–vis absorption spectra exhibit a nonmonotonic band gap variation with Mn concentration, passing through a minimum at $\sim 2\%$ Mn doping. This effect, though earlier observed in the bulk systems, is found to be more pronounced in the present case of the nanocrystals. The PL spectra of the doped samples show minor features due to Mn emission. EPR and XAS measurements establish the presence of Mn^{2+} substitutionally incorporated in the interior as well as in the surface region of the nanocrystals; the spectra are characteristic of tetrahedral Mn^{2+} species with a crystal field strength of 0.75 eV.

Acknowledgment. This work is supported by the Department of Science and Technology, Government of India. The authors gratefully acknowledge the support of the International Centre for Theoretical Physics under the ICTP-Elettra Users Programme for Synchrotron Radiation. It is a pleasure to thank the beamline scientists at the BEAR beamline of Elettra, Trieste for help with the X-ray absorption study. The authors thank Professor S. V. Bhat and Dr. Janhavi Joshi for helpful discussions on the EPR measurements.

References and Notes

- (1) Das Sarma, S. *Am. Sci.* **2001**, 89, 516.
- (2) Furdyna, J. K.; Kossut, J. *Semiconductors and Semimetals*; Academic Press: New York, 1988; Vol. 25.
- (3) Furdyna, J. K. *J. Appl. Phys.* **1988**, 64, R29.
- (4) (a) Chopra, K. L., Das, S. R., Eds. *Thin Film Solar Cells*; Plenum: New York, 1983. (b) Hingorani, S.; Pillai, V.; Kumar, P.; Multani, M. S.; Shah, D. O. *Mater. Res. Bull.* **1993**, 28, 1303. (c) Muller, J.; Fresenius, S. W. *J. Anal. Chem.* **1994**, 349, 380.
- (5) Tang, Z. K.; Wong, G. K. L.; Yu, P.; Kawasaki, M.; Ohtomo, A.; Koinuma, H.; Segawa, Y. *Appl. Phys. Lett.* **1998**, 72, 3270.
- (6) Fukamura, T.; Jin, Z.; Ohtomo, A.; Koinuma, H.; Kawasaki, M. *Appl. Phys. Lett.* **1999**, 75, 3366.
- (7) Fukamura, T.; Jin, Z.; Kawasaki, M.; Shono, T.; Hasegawa, T.; Koshihara, S.; Koinuma, H. *Appl. Phys. Lett.* **2001**, 78, 958.

- (8) Sharma, P.; Gupta, A.; Rao, K. V.; Owens, F. J.; Sharma, R.; Ahuja, R.; Osorio Guillen, J. M.; Johansson, B.; Gehring, G. A. *Nat. Mater.* **2003**, 2, 673.
- (9) Levy, L.; Hochepped, J. F.; Pileni, M. P. *J. Phys. Chem.* **1996**, 100, 18322.
- (10) Sapra, S.; Sarma, D. D.; Sanvito, S.; Hill, N. A. *Nano Lett.* **2002**, 2, 605.
- (11) Meulenkamp, E. A. *J. Phys. Chem. B* **1998**, 102, 5566.
- (12) Radovanovic, P. V.; Norberg, N. S.; McNally, K. E.; Gamelin, D. R. *J. Am. Chem. Soc.* **2002**, 124, 15192.
- (13) (a) Mahadevan, P.; Sarma, D. D. *Phys. Rev. B* **2000**, 61, 7402. (b) Sen Gupta, S.; Mahadevan, P.; Sarma, D. D. To be submitted for publication.
- (14) Bocquet, A. E.; Mizokawa, T.; Saitoh, T.; Namatame, H.; Fujimori, A. *Phys. Rev. B* **1992**, 46, 3771.
- (15) Electronic Structure Database. <http://manybody.nrl.navy.mil/esdata/database.html>.
- (16) Guinier, A. *X-ray Diffraction*; Freeman: San Francisco, CA, 1963.
- (17) Viswanatha, R.; Sapra, S.; Satpati, B.; Satyam, P. V.; Dev, B. N.; Sarma, D. D. *J. Mater. Chem.* **2004**, 14, 661.
- (18) (a) Sapra, S.; Shanthi, N.; Sarma, D. D. *Phys. Rev. B* **2002**, 66, 205202. (b) Sapra, S.; Viswanatha, R.; Sarma, D. D. *J. Phys. D: Appl. Phys.* **2003**, 36, 1595. (c) Sapra, S.; Sarma, D. D. *Phys. Rev. B* **2004**, 69, 125304.
- (19) Sapra, S.; Nanda, J.; Anand, A.; Bhat, S. V.; Sarma, D. D. *J. Nanosci. Nanotechnol.* **2003**, 3, 392.
- (20) Bylsma, R. B.; Becker, W. M.; Kossut, J.; Debska, U.; Yoder-Short, D. *Phys. Rev. B* **1986**, 33, 8207.
- (21) (a) Guo, L.; Yang, S.; Yang, C.; Yu, P.; Wang, J.; Ge, W.; Wong, G. K. L. *Chem. Mater.* **2000**, 12, 2268. (b) Guo, L.; Yang, S.; Yang, C.; Yu, P.; Wang, J.; Ge, W.; Wong, G. K. L. *Appl. Phys. Lett.* **2000**, 76, 2901.
- (22) Sakohara, S.; Ishida, M.; Anderson, M. A. *J. Phys. Chem. B* **1998**, 102, 10169.
- (23) Wong, M. E.; Searson, P. C. *Appl. Phys. Lett.* **1999**, 74, 2939.
- (24) Wu, Z. H.; Guo, L.; Li, Q. S.; Zhu, H. S. *J. Phys.: Condens. Matter* **1999**, 11, 4961.
- (25) (a) Monticone, S.; Tufeu, R.; Kanaev, A. V. *J. Phys. Chem. B* **1999**, 102, 2854. (b) Studenikin, S. A.; Golego, N.; Cociera, M. *J. Appl. Phys.* **1998**, 184, 2287.
- (26) Deshpande, C. E.; Date, S. K. *J. Mater. Sci. Lett.* **1984**, 3, 563.
- (27) Zhou, H.; Hoffmann, D. M.; Hofstaetter, A.; Meyer, B. K. *J. Appl. Phys.* **2003**, 94, 1965.
- (28) Dorain, P. B. *Phys. Rev.* **1958**, 112, 1058.
- (29) (a) de Groot, F. M. F.; Fuggle, J. C.; Thole, B. T.; Sawatzky, G. A. *Phys. Rev. B* **1990**, 42, 5459. (b) van der Laan, G.; Kirkman, I. W. *J. Phys.: Condens. Matter* **1992**, 4, 4189. (c) Nimkar, S.; Sarma, D. D.; Krishnamurthy, H. R. *Phys. Rev. B (Rapid Commun.)* **1993**, 10927, 47; (d) Hu, Z.; Golden, M. S.; Fink, J.; Kaundl, G.; Warda, S. A.; Reinen, D.; Mahadevan, P.; Sarma, D. D. *Phys. Rev. B* **2000**, 61, 3739.